Available online at www.sciencedirect.com

SciVerse ScienceDirect

Geochimica et Cosmochimica Acta 114 (2013) 220–233

Geochimica et Cosmochimica Acta

www.elsevier.com/locate/gca

Effect of carbon, sulfur and silicon on iron melting at high pressure: Implications for composition and evolution of the planetary terrestrial cores

Liwei Deng [a,b,*], Yingwei Fei [a], Xi Liu [b], Zizheng Gong [c], Anat Shahar [a]

[a] Geophysical Laboratory, Carnegie Institution of Washington, 5251 Broad Branch Road, NW, Washington, DC 20015, USA
[b] The Key Laboratory of Orogenic Belts and Crustal Evolution, Ministry of Education of China, School of Earth and Space Sciences, Peking University, Beijing 100871, China
[c] Beijing Institute of Spacecraft Environment Engineering, Beijing 100094, China

Received 1 March 2012; accepted in revised form 20 January 2013; available online 4 February 2013

Abstract

High-pressure melting experiments in the Fe–S–C ternary and Fe–S–Si–C quaternary systems have been conducted in the range of 3.5–20 GPa and 920–1700 °C in the multi-anvil press. The mutual solubility, melting relations, and crystallization sequences were systematically investigated with changes of pressure, temperature and bulk composition. Five starting materials of Fe(84.69 wt%)–C(4.35 wt%)–S(7.85 wt%), Fe(84.87 wt%)–C(2.08 wt%)–S(11.41 wt%), Fe(86.36 wt%)–C(0.96 wt%)–S(10.31 wt%), Fe(85.71 wt%)–C(0.33 wt%)–S(11.86 wt%) and Fe(82.95 wt%)–C(0.66 wt%)–S(13.7 wt%)–Si(2.89 wt%) were employed. For Fe(84.69 wt%)–C(4.35 wt%)–S(7.85 wt%), the first crystallized phase is Fe_3C at 5 GPa and Fe_7C_3 at 10–20 GPa. For Fe(84.87 wt%)–C(2.08 wt%)–S(11.41 wt%), Fe_3C is the stable carbide at subsolidus temperature at 5–15 GPa. For Fe(86.36 wt%)–C(0.96 wt%)–S(10.31 wt%) and Fe(85.71 wt%)–C(0.33 wt%)–S(11.86 wt%), the first crystallized phase is metallic Fe instead of iron carbide at 5–10 GPa. The cotectic curves in Fe–S–C ternary system indicate only a small amount of C is needed to form an iron carbide solid inner core with the presence of S. Experiments on Fe(82.95 wt%)–C(0.66 wt%)–S(13.7 wt%)–Si(2.89 wt%) showed that a small amount of C does not significantly change the closure pressure of miscibility gap compared with that in Fe–S–Si system. It is observed that S preferentially partitions into molten iron while a significant amount of Si enters the solid phase with temperature decrease. Meanwhile, the C concentration in the liquid and solid iron metal changes little with temperature variations. If S, C and Si partitioning behavior between molten iron and solid iron metal with temperature remains the same under Earth's present core pressure conditions, the solid inner core should be iron dominated with dissolved Si. On the other hand, the liquid outer core will be S rich and Si poor. Moderate carbon will be evenly present in both solid and liquid cores. Based on our melting data in a multi-component system, no layered liquid core should exist in the Earth, Mars and Mercury.

1. INTRODUCTION

The presence of light elements (~10 wt%) in the Earth's core is necessary to explain the density and velocity discrepancies between the seismic observations and the measured physical properties of pure iron. Oxygen (O), silicon (Si), sulfur (S), carbon (C) and hydrogen (H) have been suggested as potential light elements in the Earth's core based on cosmochemical and geophysical considerations (e.g., Anderson

* Corresponding author at: The Key Laboratory of Orogenic Belts and Crustal Evolution, Ministry of Education of China, School of Earth and Space Sciences, Peking University, Beijing 100871, China. Tel.: +86 10 82998419.
E-mail address: dengliwei@mail.iggcas.ac.cn (L. Deng).

0016-7037/$ - see front matter © 2013 Published by Elsevier Ltd.
http://dx.doi.org/10.1016/j.gca.2013.01.023

and Ahrens, 1994; Poirier, 1994; Anderson and Isaak, 2002; Badro et al., 2007). High-pressure experimental results, in conjunction with theoretical simulations and cosmochemical evidence, argue that it is difficult for any one of these elements to account for the core density deficit up to 10 wt% on its own (Hillgren et al., 2000). Thus it was suggested that two or more light elements might simultaneously be incorporated in the Earth's core (Poirier, 1994; Hillgren et al., 2000; Li and Fei, 2003).Sulfur is highly plausible with estimated concentrations between 2 and 14 wt%, primarily because of both its cosmic abundance and high solubility in the eutectic Fe melt at low pressure (Kuwbaschewski, 1982; Kato and Ringwood, 1989; Wood, 1993; McDonough, 2003; Li and Fei, 2003). Carbon is also cosmochemically abundant ($10 \times Si$, $20 \times S$) and present in iron meteorites. It is likely present in differentiated cores such as the Earth's core under certain conditions (Stacey and Davis, 2008; Dasgupta et al., 2013). Carbon is generally thought to be too volatile at low pressures to be maintained in the primitive Earth during the solar gas condensation process. However, it has been demonstrated by Wood (1993) that the carbon volatility is strongly pressure-dependent, and once carbon is present in a high-temperature condensed phase it is extremely nonvolatile. Silicon has been proposed as a possible light element in the core by many geophysical and geochemical arguments (e.g., O'Neil, 1991; Georg et al., 1992; Ito et al., 1995; Wänke and Dreibus, 1997; Shahar et al., 2009). It is experimentally demonstrated that silicon has significant solubility in liquid iron (25 wt% Si at the eutectic at 21 GPa, Kuwayama and Hirose, 2004) at conditions of high pressure and temperature (Lacaze and Sundman, 1991). Moreover, a Si rich Earth core could explain the super-chondritic Mg/Si in the Earth's mantle relative to chondritic meteorites, which is thought to be a first-order proxy for the bulk composition of Earth. The estimates for the concentration of Si in the core range from 2 wt% up to 14 wt% (O'Neil, 1991; Ito et al., 1995; Wänke and Dreibus, 1997). The relative high silicon concentration (14 wt%) was estimated by depletion factor of Mg/Si between the Earth and Mars based on model proposed by Wänke and Dreibus (1997).

The composition and evolution of the iron-predominant Earth's core during cooling are strictly controlled by the melting relations, subsolidus mineralogy and element partitioning of the iron-light elements system. Therefore, it is critical to understand the melting behavior of Fe alloying with light elements at high pressure and temperature. Geochemical evidences suggest 0.2–4 wt% carbon concentration in the Earth's bulk core (Wood 1993; McDonough and Sun, 1995). Recently, high pressure carbon partition study suggested that a 0.2–0.25 wt% carbon concentrated Earth's core (Dasgupta et al., 2013), assuming ~730 ppm carbon was available during early Earth differentiation (McDonough, 2003). There have been several experimental studies on the melting behavior of the Fe–S–C ternary system up to 6 GPa (Corgne et al., 2008; Dasgupta et al., 2009). However, the carbon concentrations in previous synthetic starting compositions, spanning from 3.2 wt% to carbon-saturated conditions, may be much higher than the anticipated concentration in the Earth's core. In this work we extended high-pressure melting experiments in the Fe–S–C system up to 20 GPa by using the multi-anvil press. We also examined the effect of carbon on the Fe–FeS melting relations and crystallization sequences with carbon concentrations ranging from 0.3 to 4 wt%. Furthermore, based on the Fe–S–C ternary melting relations, silicon was added to extend the discussion on the mutual solubility of carbon, sulfur and silicon and crystallization behavior in the Fe–S–C–Si quaternary system. The results provide insights into the composition and evolution of planetary cores.

2. EXPERIMENTAL AND ANALYTICAL PROCEDURES

High-pressure experiments were performed at 3.5–20 GPa and 920–1700 °C in two Walker-type multi-anvil presses (either 800-ton or 1500-ton press) installed at the Geophysical Laboratory (Bertka and Fei, 1997; Fei et al., 1997). The 10/5 and 8/3 assemblages (edge length of the octahedron/truncated edge length of the WC anvil) were used in the multi-anvil experiments. Sintered MgO and boron nitride (BN) capsules were used as the sample containers for Fe–S–C and Fe–S–C–Si starting materials, respectively. The sample was heated by a cylindrical Re furnace. ZrO_2 and $LaCrO_3$ were used as the thermal insulator for the 10/5 and 8/3 assemblies, respectively. All the cell parts were treated at 1000 °C for 12 h before they were assembled. In some experiments, two samples separated by a layer of MgO powder were simultaneously loaded. Temperatures were determined using a W5%Re–W26%Re thermocouple without any correction for the effect of pressure on the emf. The temperature gradient over the length of the sample chamber (<500 μm) was approximately 20 °C (Fei et al., 2000). Oil pressure was calibrated using the phase boundaries of pyroxene–majorite, coesite-stishovite and olivine–wadsleyite (Bertka and Fei, 1997; Fei et al., 1997).

Starting materials were prepared as mechanical mixtures of iron, graphite, FeSi and FeS (99.99% pure; Alfa Aesar product). The mixtures were ground for 30 min in ethanol using an agate mortar and pestle to ensure the homogeneity and fine grain size. For the Fe–S–C samples, four starting materials with different carbon and sulfur concentrations were prepared: a, Fe(84.69 wt%)–C(4.35 wt%)–S(7.85 wt%); b, Fe(84.87 wt%)–C(2.08 wt%)–S(11.41 wt%); c, Fe(86.36 wt%)–C(0.96 wt%)–S(10.31 wt%); and d, Fe(85.71 wt%)–C(0.33 wt%)–S(11.86 wt%) (hereafter termed as Fe84.69–C4.35–S7.85, Fe84.87–C2.08–S11.41, Fe86.36–C0.96–S10.31 and Fe85.71–C0.33–S11.86, respectively). For the Fe–S–C–Si sample, we prepared a starting material with Fe(82.95 wt%)–C(0.66 wt%)–S(13.7 wt%)–Si(2.89 wt%) (hereafter termed as Fe82.95–C0.66–S13.7–Si2.89). It is hard to control the carbon concentration during the sample preparation and iron loss to the capsule during the run. The final bulk compositions were obtained by analyzing the quenched homogenous melt without the presence of graphite/diamond from experimental runs (PL-245, m-1022, m-1019 and m-1033, LO-706a and LO-704, LO-706b, m-1161 and PR899). The uncertainties in the measured compositions of the starting materials are largely due to the heterogeneity of the quenched texture.

The sample was pressurized at room temperature to the target pressure and then heated to the desired temperature at a rate of 100 °C/min. Metallurgic ambient experiment demonstrates that a heating duration of 4 h was sufficient to approach chemical equilibrium for the Fe–S–C system (Wang et al., 1991). Because pressure usually elevates the melting temperature, we extended the heat duration to 6 h to ensure thermodynamic equilibrium at high pressures. The same duration of heating was applied for the Fe–S–C–Si system runs. The samples were quenched by switching off the power directly. It took less than 2 s to cool down from a temperature over 1000 °C to less than 200 °C. After decompression, the samples were recovered, mounted in silver epoxy, and carefully mechanically polished. The polished samples were analyzed with a JEOL8900L electron microprobe with operation conditions of 15 kV and 20 nA. To avoid carbon-coating effect on the quantitative analysis of carbon, the samples were not carbon-coated. Carbon lines were drawn at the edge of the sample to the sample holder to allow charge transfer during analysis. The solid and liquid phases were analyzed using a spot beam (with a diameter less than 3 μm) and area scanning (20 μm × 20 μm), respectively. Fe, S and Si were analyzed by wavelength dispersive spectrometry employing analytical standards of NIST pure iron 2168, pyrite (FeS_2) and enstatite ($MgSiO_3$). The presence of oxygen in the samples was detected by EDAX peak search, and oxygen was analyzed employing standard of MgO for run products in the Fe–S–C system and $MgSiO_3$ for run products in the Fe–S–C–Si system. Spectrometer crystals were LiTH for Fe, LDE2 for C, PETJ for S, TAP for Si and LDE1 for O. The textures of the quenched samples were examined by back-scattered electron imaging. Polycrystalline X-ray diffraction data were also used for phase identification.

It's well known that carbon measurements encounter many practical problems, in particular because the X-ray emission of carbon is low and the absorption of C Kα radiation is high in different matrices (Bastin and Heijligers, 1986; Pouchou, 1996; Goldstein et al., 1992). Some other problems arise from inevitable cracking of residual organic molecules, coming from vacuum grease and residual oil vapors of the diffusion pump oil in the microprobe chamber, under the action of the electron beam and then progressive buildup on the surface of sample during analysis cycle (Wood, 1993; Robaut et al., 2006; Dasgupta and Walker, 2008). In this study, we established a calibration curve for the C Kα line intensity at the maximum of the peak as a function of carbon content using different standards. The method is an efficient way to measure carbon content even at low concentration (range 0–1 wt%) (Robaut et al., 2006). The calibration curve for the C Kα line intensity was based on NIST steels with 0.0, 0.215, and 0.969 wt% carbon and a synthetic cohenite (Fe_3C) (6.7 wt% carbon). In order to improve measuring precision, C Kα peak position search was performed by analyzing Fe_3C on LDE2 for each probe cycle. The carbon calibration lines were established for each set of measurements. These calibration lines produce very consistent intensity-carbon content relations (Fig. 1). As an additional precaution, most samples were preceded duplicate or triplicate analyses during different analysis cycles to ensure self-consistency. During measurement process we observed that NIST 337a (0.969 wt% C) and NIST 19 h (0.215 wt% C) are easily oxidized when exposed in air. Therefore, standards and all samples were carefully re-polished and then ultrasonically cleaned in ethanol each time just before loading into the microprobe chamber.

To ensure the quality of data, we discarded those samples, which were heated manually by applying the calibrated temperature–power curve or for which heating duration was less than 6 h. We also discarded samples contaminated by Re and W elements from the thermocouple wire. As an interesting observation, W preferentially partitions into the Fe–C dendrites upon quenching rather than the Fe–S melt.

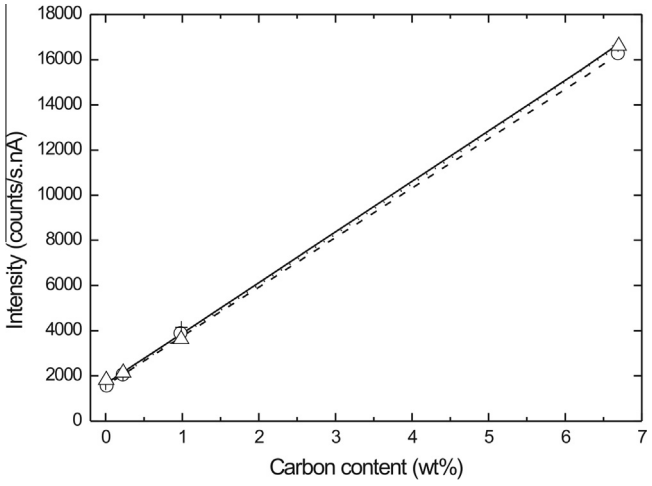

Fig. 1. Calibration curves of carbon concentration obtained at 15 keV and 20 nA with pure iron, two NIST steels (0.969 and 0.215 wt% carbon) and a synthetic cohenite (Fe_3C) (6.7 wt% carbon) in three different probe sessions. The carbon content of the measured sample is simply calculated from the regression curve coefficients A and B (intensity $= A \times$ wt% $+ B$) with $\sigma(A) = 0.02$, $\sigma(B) = 0.04$.

Table 1
Experimental conditions, phase observations and phase compositions for Fe–C–S system determined by electron probe microanalysis (wt%).

Run #	*P* (GPa)	*T* (°C)	Phase	Fe	C	S	O	Total
(a) Starting composition Fe84.69–C4.35–S7.85								
m-1006[e]	3.6	920	Fe	99.23 (31)[f]	0.82 (9)	0.56 (20)	0.48 (18)	101.10 (17
			Fe_3C	92.47(186)	6.79(21)	0.04(03)	2.82(225)	102.12(49)
			FeS	62.38	0	34.88	3.23	100.48
m-1010	3.5	1500	Fe_3C	93.02(23)	6.70(13)	0.01(1)	0.08(4)	99.81(32)
			Melt	86.92(81)	2.96(34)	8.39(109)	0.52(16)	98.80(24)
			Graphite[g]					
m-1012	3.5	1600	Fe–C melt	85.79 (32)	5.67(33)	4.71(36)	3.124(25)	99.29(48)
			Fe–S melt	64.69 (84)	1.36(51)	31.24(63)	2.423(29)	99.71(54)
			Graphite[g]					
m-997	5	1200	Fe	97.32(153)	1.22(14)	0.34(54)	0.94(59)	99.82(56)
			Fe_3C	93.11(23)	6.87(12)	0.03(8)	0.1(3)	100.10(23)
			FeS	60.61(71)	1.28(41)	32.83(220)	3.23(168)	98.82(35)
m-1002	5	1350	Fe_3C	93.10(34)	6.44(30)	0.01(1)	0.14(13)	99.70(44)
			Melt	76.69(21)	0.18(2)	20.93(4)	0.49(8)	98.29(24)
m-998	5	1500	Melt	89.70(50)	3.02(22)	6.17(62)	0.53(11)	99.42(25)
			Graphite[g]					
PL-253	10	1025	Fe_7C_3	91.26(30)	8.47(58)	0.15(32)	0.44(21)	100.32(32)
			FeS	62.90(12)	0	36.26(14)	0.21(23)	99.30(19)
			Fe[i]					
m-1097	10	1100	Fe_7C_3	91.16(21)	7.94(62)	0.14(17)	0.37(19)	99.62(64)
			FeS	63.48	0.12	33.92	0.51	98.04
			Fe[h]					
m-1101	10	1200	Fe_7C_3	91.37(17)	8.43(8)	0.04(1)	0.05(3)	99.89(19)
			Fe[i]					
			Melt	76.99(84)	0.24(11)	20.73(78)	0.48(13)	98.44(20)
m-1014	10	1500	Fe_7C_3	91.77(79)	8.44(21)	0.03(1)	0.05(2)	100.28(38)
			Melt	84.87(79)	2.69(22)	11.46(32)	0.48(10)	99.50(51)
m-1018	10	1600	Fe_7C_3	91.46(12)	8.21(11)	0.03(1)	0.18(9)	99.87(20)
			Melt	85.96(132)	2.53(104)	10.65(227)	0.28(6)	99.42(23)
m-1040	10	1700	Melt	86.63(97)	3.16(65)	8.37(54)	0.75(8)	98.90(28)
			Graphite[h]					
LO-707	15	1050	Fe	94.23	4.19	0.95	2.66	102.02
			Fe_7C_3	92.97(40)	7.04(42)	0.15(19)	0.18(12)	100.33(29)
			Fe_3S_2	69.56(67)	0.47(28)	28.26(75)	1.38(115)	99.66(29)
LO-705a	15	1150	Fe_7C_3	91.71(34)	8.22(26)	0.08(4)	0.20(11)	100.20(54)
			Melt	83.62(85)	1.49(10)	14.36(91)	0.42(6)	99.89(32)
LO-701a	15	1250	Fe_7C_3	92.17(21)	8.14(22)	0.06(1)	0.13(4)	100.50(37)
			Melt	85.45(174)	2.47(74)	11.78(168)	0.59(21)	100.30(36)
LO-708a	15	1450	Fe_7C_3	91.55(1)	8.22(31)	0.05(1)	0.05(2)	99.87(36)
			Melt	85.38(193)	2.33(82)	11.00(274)	0.30(8)	99.00(27)
LO-709	15	1550	Melt	88.20(9)	2.67(7)	9.38(17)	0.23(6)	100.48(5)
			Graphite[h]					
PL-249	20	1100	Fe_7C_3	90.43(49)	9.39(62)	0.10(2)	0.34(10)	100.26(39)
			Fe_3S_2	70.58(39)	0.89(10)	27.48(15)	0.79(5)	99.73(31)
			Fe[i]					
PL-440	20	1175	Fe_7C_3	94.14(29)	7.43(63)	0.04(0)	0.10(4)	101.71(44)
			Fe[i]					
			Melt	79.20(34)	0.00(19)	20.10(25)	0.33(7)	99.62(23)
PL-252	20	1250	Fe_7C_3	91.92(37)	8.41(50)	0.09(1)	0.39(19)	100.81(61)
			Fe[i]					
			Melt	80.16(94)	0.41(12)	18.59(53)	0.59(29)	99.76(47)
PL-246	20	1400	Fe_7C_3	91.79(55)	8.39(37)	0.08(1)	0.40(16)	100.66(68)
			Melt	83.25(202)	1.86(28)	13.55(175)	1.39(35)	100.04(54)
PL-254	20	1475	Fe_7C_3	90.92(27)	8.67(30)	0.08(1)	0.22(1)	99.88(15)
			Melt	84.70(74)	1.95(44)	11.50(88)	0.74(13)	98.89(28)
PL-256	20	1500	Melt	89.22(105)	3.61(35)	6.11(129)	0.58(11)	99.53(31)
			Graphite[g]					
PL-245	20	1550	Melt	84.69(22)	4.35(6)	7.84(38)	2.06(13)	98.95(38)

(*continued on next page*)

Table 1 (*continued*)

Run #	*P* (GPa)	*T* (°C)	Phase	Fe	C	S	O	Total
(b) Fe84.87–C2.08–S11.41								
m-1023	5	1100	Fe	98.58(65)	0.87(13)	0.31(57)	0.45(12)	100.21(34)
			Fe_3C	92.69(43)	7.17(36)	0.12(12)	0.44(40)	100.43(29)
			FeS	62.47(27)	0.04(4)	36.02(2)	0.20(20)	98.73(19)
m-1024	5	1200	Fe	98.56(22)	1.21(15)	0.03(1)	0.10(1)	99.90(18)
			Fe_3C	93.34(30)	6.41(13)	0.01(1)	0.06(1)	99.82(31)
			Melt	81.83(130)	0.61(31)	15.99(134)	0.49(6)	98.92(18)
m-1022	5	1400	Melt	84.73(149)	2.13(7)	11.60(110)	0.54(28)	99.00(23)
m-1019	5	1600	Melt	85.87(148)	2.07(31)	10.35(156)	0.55(6)	98.84(32)
m-1029	10	1200	Fe	98.62(153)	0.67(14)	0.59(133)	0.53(16)	100.41(20)
			Fe_3C	92.16	6.73	1.12	0.11	100.12
			FeS	62.99(56)	0.04(18)	36.22(77)	0.08(4)	99.32(23
m-1036	10	1350	Fe_3C	93.07(19)	6.63(11)	0.02(1)	0.13(3)	99.85(28)
			Melt	84.09(44)	1.18(46)	13.07(101)	0.71(12)	99.06(7)
m-1033	10	1400	Melt	84.02(32)	2.03(15)	12.26(38)	0.64(15)	98.31(18)
LO-705b	15	1150	Fe	98.42(122)	1.69(36)	0.05(1)	0.35(40)	100.52(46)
			Fe_3C	93.17(16)	6.51(34)	0.14(17)	0.19(4)	100.00(23)
			Melt	82.95(121)	0.47(15)	15.73(133)	0.42(10)	99.58(29)
LO-701b	15	1250	Fe_3C	93.30(35)	6.57(16)	0.04(0)	0.25(34)	100.15(26)
			Melt	78.70(154)	0.13(4)	19.09(85)	1.09(76)	99.01(17)
			Fe[i]					
LO-700	15	1350	Fe_3C	93.61(38)	6.79(30)	0.03(2)	0.16(14)	100.58(24)
			Melt	85.63(66)	2.00(16)	11.81(69)	0.62(7)	100.06(16)
LO-708b	15	1450	Melt	89.34(60)	3.04(40)	7.31(71)	0.31(7)	100.00(14)
			Graphite[g]					
(c) Fe86.36–C0.96–S10.31								
m-1093a	5	1100	Fe	98.85(34)	1.27(12)	0.02(1)	0.14(2)	100.29(40)
			FeS	63.27(107)	0.59(37)	35.81(157)	0.34(24)	100.01(16)
			Fe_3C	92.99(37)	7.32(22)	0.01(0)	0.14(1)	100.47(39)
m-1089a	5	1300	Fe	99.00(10)	0.61(3)	0.05(1)	0.13(2)	99.80(10)
			Melt	85.96(108)	0.85(1)	11.75(92)	0.44(11)	99.00(23)
LO-703a	10	1000	Fe	99.17(66)	0.58(11)	0.27(26)	0.29(18)	100.31(23)
			FeS	62.84(130)	0.05(12)	35.69(88)	0.47(17)	99.04(104)
			Fe_3C	92.25(115)	6.89(18)	0.60(77)	0.46(23)	100.20(73)
LO-706a	10	1200	Melt	87.30(97)	1.00(9)	9.59(85)	0.78(9)	98.67(31)
LO-704	10	1300	Melt	87.23(148)	1.33(59)	9.61(11)	0.52(39)	98.68(39)
(d) Fe85.71–C0.33–S11.86								
m-1093b	5	1100	Fe	98.46(76)	0.28(16)	0.98(7)	0.46(7)	100.18(23)
FeS				62.49(22)	0.91(104)	36.61(19)	0.19(7)	100.20(70)
m-1088	5	1200	Fe	98.69(20)	1.29(25)	0.03(1)	0.16(2)	100.17(32)
			Melt	81.14(83)	0.73(13)	16.93(75)	0.63(6)	99.42(5)
m-1095	5	1225	Fe	93.01	1.41	3.31	1.86	99.57
			Melt	84.72(79)	0.52(23)	13.38(67)	1.00(13)	99.62(21)
m-1089b	5	1300	Fe	98.68(85)	0.45(13)	0.27(51)	0.26(22)	99.65(37)
			Melt	88.47(92)	0.62(8)	9.38(90)	0.41(6)	98.88(20)
LO-703b	10	1000	Fe	99.10(15)	0.41(7)	0.33(18)	0.65(8)	100.48(3)
			FeS	62.47(15)	0	36.17(22)	0.16(5)	98.74(20)
LO-706b	10	1200	Melt	85.71(78)	0.33(17)	11.86(63)	1.11(22)	99.02(22)

In some runs, two different samples were loaded in separate capsules for one run. a and b were labeled after run number to distinguish different samples.

[e] m-1006 was performed by 18/11 assembly using graphite heater.

[f] 99.23(31) should be read as 99.23 ± 0.31. In some cases standard deviations are absent due to the unavailability of appropriate area for electron probe microanalysis.

[g] Either graphite or diamond is observed.

[h] Either graphite or diamond is required by mass balance.

[i] Missing Fe reacted with MgO capsule.

3. RESULTS

A series of experiments were conducted between 3.5 and 20 GPa and at temperatures up to 1700 °C, by using five different starting compositions. Melting relationships were interpreted based on the quenched textures described by Fei et al. (1997): intergrowth of different solid phases with clear grain boundaries shows subsolidus reaction while dendritic texture is indicative of melting. Immiscible liquids can be identified by the appearance of droplets dispersed in a liquid matrix. Due to the reaction of the MgO capsule and the Fe in the starting material, a reaction boundary of (Mg,Fe)O formed surrounding the sample in the Fe–S–C system. The observed phase assemblages and the chemical compositions are summarized in Tables 1 and 2.

3.1. Phase relations in composition Fe84.69–C4.35–S7.85

Fig. 2a shows the typical immiscible phenomenon of two melts at 3.5 GPa and 1600 °C, characterized by dispersing of the Fe–S droplets with diameter less than 10 μm into the Fe–C melt matrix. This observation is consistent with existing experimental results (Wang et al., 1991; Wood, 1993; Corgne et al., 2008; Dasgupta et al., 2009). Considering the initial compositions with similar S/C ratio were used in studies of Corgne et al. (2008) (3.2–3.8 wt% C, 6.09–7.22 wt% S) and Dasgupta et al. (2009) (5 wt% C–5 wt% S) compared with ours (4.35 wt% C–7.85 wt% S), the carbon contents of the immiscible melts (1.36 wt% in the Fe–S melt and 5.67 wt% in the Fe–C melt) are generally in good agreement with the reported values of Corgne et al. (2008) and Dasgupta et al. (2009). However, the S content in the Fe–C (4.7 wt%) melt is higher than the result (~2.5 wt%) of Corgne et al. (2008). The differences may reflect the effect of temperature. At the top end of the sample chamber graphite crystals were observed, coexisting with the Fe–C melt. Nakajima et al. (2009) observed two different graphite textures (platen, and petaline and acicular) in their quenched Fe–C sample at 5 GPa and 1400 °C. With a time-dependent study at specified pressure and temperature, they interpreted that platen graphite was a stable phase coexisting with molten iron prior to quenching whereas the petaline and acicular graphite were precipitation from melt during quenching. Based on the texture observation and mass balance consideration, we suggest that the graphite crystal in our experiment is an equilibrium phase.

Only one melt with the dendritic texture was observed at 5 GPa and 1500 °C, indicating the complete closure of the miscibility gap of two melts (Fig. 2b). Therefore, the closure pressure for miscibility gap is constrained at ~4.9 GPa with composition of 3.2–5 wt% C and 5–7.22 wt% S considering reported closure pressures of Corgne et al. (2008) (4.8–6.2 GPa) and Dasgupta et al. (2009) (4–6 GPa).The experimental temperatures in these three studies ranged from 1400 to 2200 °C; similar closure pressures of the miscibility gap at very different temperatures might suggest that temperature has a very limited effect, potentially in conflict with the suggestion of lower closure pressure at higher temperature (Wood, 1993). Quench texture was clearly observed as small vesicles in the melt matrix (Fig. 2b). These vesicles might be caused by the escape of the dissolved oxygen in the melts or the volume extraction of liquid upon quenching. At 5 GPa, upon cooling to 1350 °C Fe_3C crystallizes first, coexisting with the Fe–S melts (Fig. 2c). The abundance of S and C in the Fe–S melts is 20.93 and 0.18 wt%, respectively. At the lowest experimental temperature (1200 °C), Fe_3C intergrowths with FeS and Fe, representing the subsolidus phase assemblage (Fig. 2d). This solidus temperature, placed between 1200 and 1350 °C, is higher than the eutectic temperature in the Fe–FeS binary system, but lower than that in the Fe–C binary system at the same pressure (Fei et al., 1997, 2007; Lord et al., 2009; Buono and Walker, 2011).

We observed another iron carbide phase (Fe_7C_3) at 10 GPa and higher pressures. The carbon content in this starting composition is sufficiently high so that Fe_7C_3 becomes the dominant iron carbide in our experiments. The appearance of Fe_7C_3 is also consistent with observation of breaking down of Fe_3C into Fe_7C_3 and melt at 6 GPa (Dasgupta et al., 2009). With increasing pressure, the subsolidus phase assemblages change from Fe–Fe_3C–FeS at 5 GPa to Fe–Fe_7C_3–FeS at 10 GPa and then to Fe–Fe_7C_3–Fe_3S_2 at 15 GPa (Table 1). The formations of Fe_7C_3 and Fe_3S_2 at higher pressures are consistent with

Table 2
Experimental conditions, phase observations and phase compositions for Fe–C–S–Si system determined by electron probe microanalysis (wt%).

Run #	*P* (GPa)	*T* (°C)	Phase	Fe	C	S	Si	O	Total
Starting composition Fe82.95–C0.66–S13.7–Si2.89									
m-1154	5	1300	Fe–Si solid	87.39(46)	0.14(7)	0.02(1)	12.42(41)	0.28(14)	100.25(52)
			Melt	78.22(79)	0.67(20)	18.14(91)	2.24(17)	0.32(8)	99.59(33)
PR901	5	1350	Fe–S melt	78(1.57)	0.06(14)	18.46(2.33)	3.13(78)	0.65(22)	100.30(11)
			Fe–Si melt	82.51(97)	0.21(19)	12.10(1.39)	4.88(22)	0.41(16)	100.11(8)
PR899	5	1400	Melt	82.64(71)	0.32(22)	12.92(1.08)	3.87(18)	0.50(38)	100.25(43)
m-1162	10	1200	Fe–Si solid[j]						
			Melt	83.30(1.55)	0.22(4)	13.64(1.92)	2.85(49)	0.22(13)	100.22(16)
m-1164	10	1275	Fe–Si solid	89.68(29)	0.07(14)	0.06(1)	10.65(22)	0.23(11)	100.69(22)
			Melt	86.91(1.5)	0.21(16)	7.97(1.7)	5.40(65)	0.11(2)	100.60(23)
m-1161	10	1350	Melt	83.26(1.59)	1.00(59)	14.47(1.88)	1.90(54)	0.21(6)	100.85(81)

[j] Composition not determined due to the unavailability of appropriate area for electron probe microanalysis and EDX is used to identify the major compositions qualitatively.

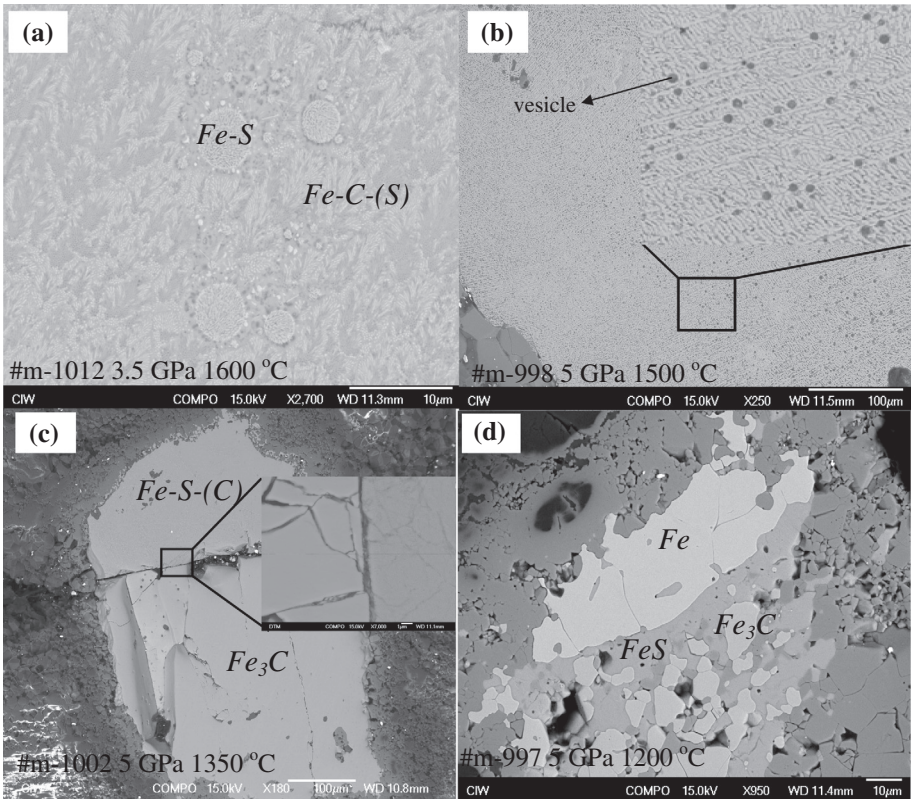

Fig. 2. Scanning electron microscope composition images of the quenched samples at different P and T conditions. (a) Sample m-1012 shows two immiscible liquids (S-rich and C-rich melts) at 3.5 GPa and 1600 °C. Fe–S drops (bright spheres) with diameter less than 10 μm disperse into C-rich iron liquid. A layer of (Mg, Fe)O was observed between the melt and the MgO capsule. Graphite (black) was also observed at the edge of sample chamber as stable phase. (b) m-998 shows one homogenous melt with dendritic texture at 5 GPa and 1500 °C, which indicates complete closure of miscibility gap. Many small vesicles (black dots in the enlarged image) were observed in the quenched melt. These vesicles may result from the escape of the dissolved oxygen in the melts during temperature quenching. (c) m-1002 shows solid Fe_3C coexists with Fe–S melt at 5 GPa and 1350 °C. (d) m-997 shows subsolidus phase assemblage (Fe_3C, FeS, and pure Fe) at 1200 °C and 5 GPa.

their being the dominated iron-carbide and iron-sulfide phase in the Fe–C and Fe–FeS binary systems, respectively (Shterenberg et al., 1975; Wood, 1993; Fei et al., 1997). Partial melting at 10 GPa starts at a temperature between 1100 and 1200 °C (Table 1). On the other hand, the liquidus temperature is significantly high (1700 °C) at 10 GPa (m-1040), with graphite/diamond as the liquidus phase. As pressure increases, partial melting starts between 1050 and 1150 °C at 15 GPa, and 1100 and 1175 °C at 20 GPa. This observation is consistent with the experimental result that the solidus temperature decreases slightly with pressure increasing in Fe–S system (Fei et al., 1997).

We investigated the carbon and sulfur contents in the melts, which coexist with Fe_7C_3 at different temperatures. The abundances of carbon increase slightly with increasing temperature at a given pressure (Fig. 3). This indicates the steep slope of liquidus temperature of Fe_7C_3 + (S rich) Liquid in X (composition) − T space. On the contrary, sulfur concentrations decrease significantly with increasing temperatures. The sulfur is strongly concentrated in the liquid. Therefore, sulfur content in the melts is primarily controlled by the volume proportion of the melt, so that it decreases with increasing temperature. On the other hand, the carbon content in the melts is mainly controlled by carbon partitioning between melt and solid, and slightly increases with increasing temperature at a given pressure. As shown in Fig. 3, our data are broadly consistent with the reported 6 GPa result from Dasgupta et al. (2009). The influence of pressure on the melt composition appears less systematic possibly because of the significant change of the eutectic composition as a function of pressure.

3.2. Phase relations in composition Fe84.87–C2.08–S11.41

With decreasing carbon content in the starting material, Fe_7C_3 is not stable any more. For the investigated pressure interval, the subsolidus phase assemblage is Fe–Fe_3C–FeS, and FeS remains as the first phase to melt (m-1024 at 5 GPa, m-1036 at 10 GPa and LO-705b at 15 GPa). The solidus temperatures at 5 and 10 GPa show little change (1200 ± 50 °C; Table 1), as do the liquidus temperatures (1350 ± 50 °C). Metallic iron was observed in m-1024 and LO-705b and it coexists with Fe_3C at the bottom of the sample chamber (Fig. 4a).

In comparison, both compositions Fe84.87–C2.08–S11.41 and Fe84.69–C4.35–S7.85 have similar solidus temperature at 5, 10 and 15 GPa respectively (∼1200 °C at 5 and 10 GPa, ∼1150 °C at 15 GPa), reflecting the fact that the S-bearing solid phase (either FeS or Fe_3S_2) is the first phase to melt. The liquidus temperatures are somewhat dif-

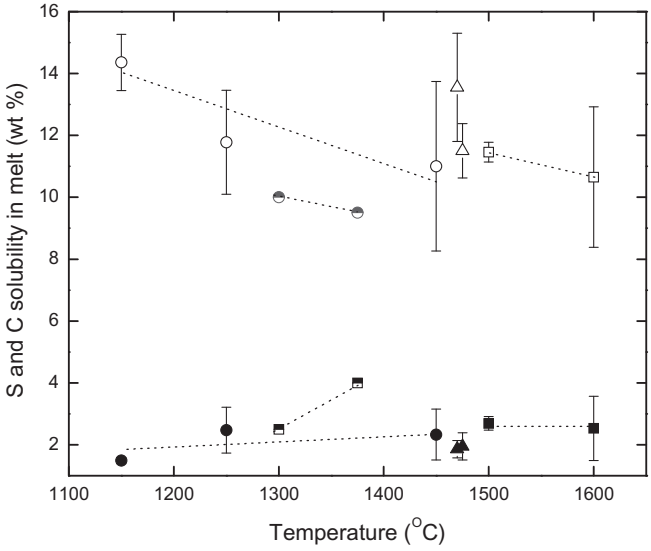

Fig. 3. Solubility of S and C in Fe–S melt which coexists with solid Fe_7C_3 as a function of temperature for composition Fe84.69–C4.35–S7.85. Open squares, circles and triangles represent the S contents in the melts at 10, 15 and 20 GPa, respectively. And the solid symbols represent the C contents in the melts at the corresponding pressures. The halffilled symbols are the S and C solubility at 6 GPa from Dasgupta et al. (2009). The dotted lines are for visual guide only.

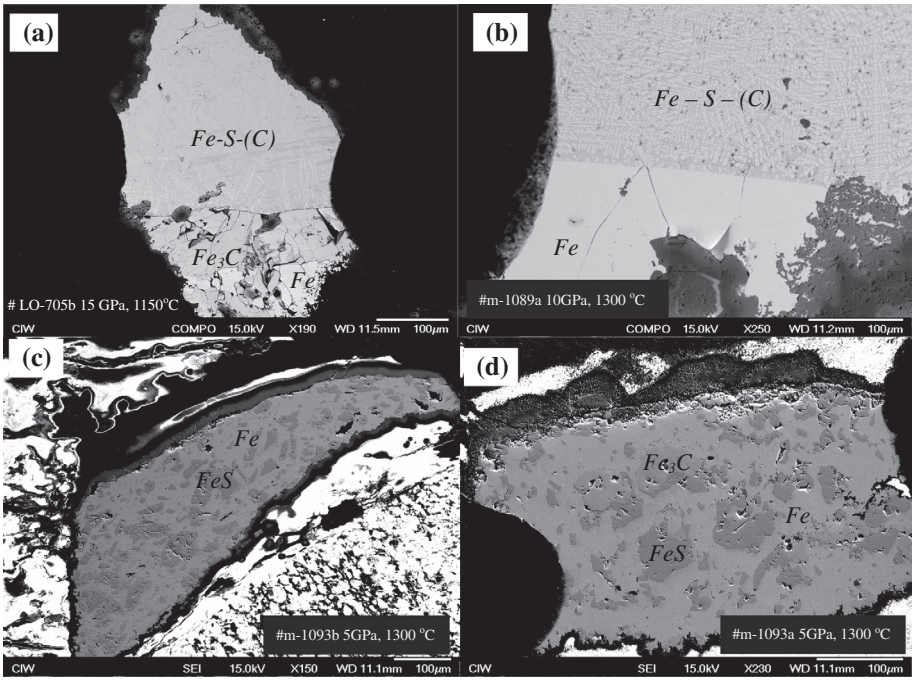

Fig. 4. Scanning electron microscope composition images of the quenched samples. (a) LO-705b (15 GPa and 1150 °C) shows coexistence of iron and Fe_3C at the cool end of the sample chamber, whereas Fe_3C coexists with Fe–S melt at the hot end, indicating the experimental temperature is close to the solidus. (b) m-1089a shows C-bearing metallic iron coexists with Fe–S melt at 10 GPa and 1300 °C. (c) m-1093b shows subsolidus phase assemblage of iron and FeS at 5 GPa and 1100 °C for Fe85.71–C0.33–S11.86. (d) m-1093a shows subsolidus phase assemblage of Fe-–Fe_3C–FeS at 5 GPa and 1100 °C for Fe86.36–C0.96–S10.31.

ferent: that for Fe84.69–C4.35–S7.85 (1350–1500 °C at 5 GPa, 1600–1700 °C at 10 GPa, 1450–1550 °C at 15 GPa) is about 100 °C higher than that for Fe84.87–C2.08–S11.41 (1200–1400 °C at 5 GPa, 1350–1400 °C at 10 GPa, 1350–1450 °C at 15 GPa) at given pressure. This is consistent with the experimental result that the melting point of Fe_7C_3 is higher than that of Fe_3C (Lord et al., 2009).

The experimental results with composition Fe84.87–C2.08–S11.41 can be compared to those in the system Fe–C. For the Fe–C binary system at 10 GPa, Fe is the

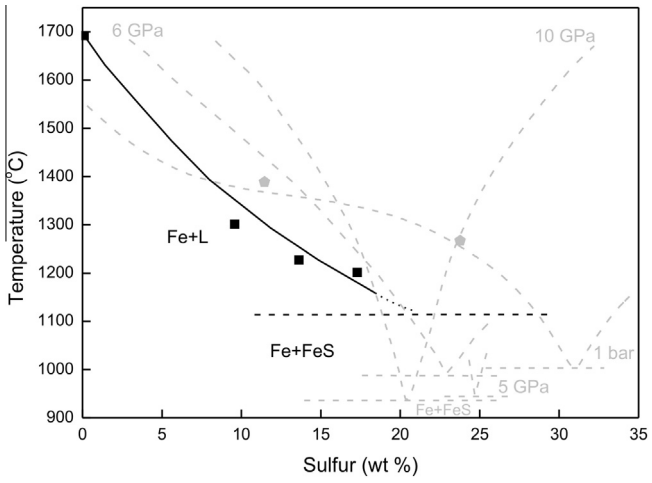

Fig. 5. Schematic T–X diagram in the Fe–S–C system. The sulfur and iron contents (m-1088, m-1095 and m-1089b) of the melts are renormalized to 100%. The melting relations at 1 bar and 10 GPa are from Fei et al. (1997). And the 6 GPa and hypothetical 5 GPa melting curve are from Buono and Walker (2011) and Chudinovskikh and Boehler (2007), respectively. Thin curves are for the Fe–S system while thick curves for the Fe–S–C system.

liquidus phase with carbon concentrations up to 4.2 wt% in the melt (Lord et al., 2009); in contrast, Fe_3C crystallizes first in the Fe–S–C system with carbon concentration as low as 1.18 wt% (m-1036; 10 GPa). The change of the liquidus phase under the same pressure from Fe in the Fe–C binary system to Fe_3C in the Fe–S–C at similar carbon concentrations suggests that the eutectic composition is significantly modified with the addition of S into the system.

3.3. Phase relations in compositions Fe86.36–C0.96–S10.31 and Fe85.71–C0.33–S11.86

By further reducing the carbon content in the starting material, it is expected that the liquidus phase should change from iron carbide to metallic iron. Figure 4b shows that at 5 GPa metallic iron is indeed the liquidus phase for both Fe86.36–C0.96–S10.31 and Fe85.71–C0.33–S11.86. This is fundamentally important as it indicates compositions of Fe86.36–C0.96–S10.31 and Fe85.71–C0.33–S11.86 lie on the other side of the eutectic point compared with the C-rich compositions (Fe84.69–C4.35–S7.85 and Fe84.87–C2.08–S11.41) when projecting them on the Fe–C phase diagram at given pressure. In addition, with low carbon concentration in the bulk composition (e.g. Fe85.71–C0.33–S11.86), all carbon is dissolved in metallic iron, forming the subsolidus phase assemblage Fe + FeS (Fig. 4c). With increasing carbon concentration (e.g., Fe86.36–C0.96–S10.31), excess carbon becomes available to form iron carbide, and the subsolidus phase assemblage becomes Fe + FeS + Fe_3C (Fig. 4d) or Fe + FeS + Fe_7C_3 (Table 1). Even thought there is ~50 °C difference in Fe–S solidus temperatures reported by Chudinovskikh and Boehler (2007) and Buono and Walker (2011), the effect of a small amount of carbon on the solidus of the system Fe + S still seems rather significant (Fig. 5): at 5 GPa, the addition of 0.33 wt% C into the system elevates the solidus by approximately 150 °C. It seems the eutectic composition in the normalized Fe–S–C system is quite comparable with that in Fe–S system taking into the account of the measurement error.

3.4. Phase relations in compositions Fe87.81-C0.99-S14.62-Si6.57

To obtain a more realistic Earth core composition, silicon was added to the Fe–S–C ternary system to extend further discussion on the mutual solubility and crystallization behavior in the Fe–S–C–Si quaternary system.

At 5 GPa, a solid Fe (+12.42 wt% Si) coexisting with S rich liquid was observed at 1300 °C. As an interesting observation, a silicon rich droplet was observed in the S rich liquid (Fig. 6a). The composition is 87.81 wt% (Fe)–0.99 wt% (C)–4.62 wt% (S)–6.57 wt% (Si)–0.42 wt% (O), which is significantly different with the that of coexisting liquid. However, no such similar droplet was found elsewhere in this sample. With increasing temperature (to 1350 °C), two immiscible liquids, S-rich melt and Si-rich melt, were preserved in the quenched melt (Fig. 6b). The observed Fe–S and Fe–Si immiscible liquids texture is different from that in Fig. 2a: the Si rich melt formed open circle emulsions rather than the generally described characteristic egg-like texture (Sanloup and Fei 2004; Morard and Katsura, 2010). This may due to the high iron content in Si rich melt suggested by Morard and Katsura (2010). SiO_2 grains formed due to the oxidation of the starting materials, which lowers the Si content in the bulk starting composition. With further increasing temperature, the miscibility gap closed at 1400 °C (PR-899).

At 10 GPa, only one homogenous dendritic texture was observed at 1350 °C (m-1161), indicating the closure of the miscibility gap. Therefore, the closure pressure for miscibility gap between Fe–Si and Fe–S melts in Fe–S–Si–C quaternary system is constrained between 5 and 10 GPa. The pressure at which miscible gap occurred and closed in this study achieves a good agreement with observation in Fe–Si–S system (Morard and Katsura, 2010). Therefore, adding a small amount of

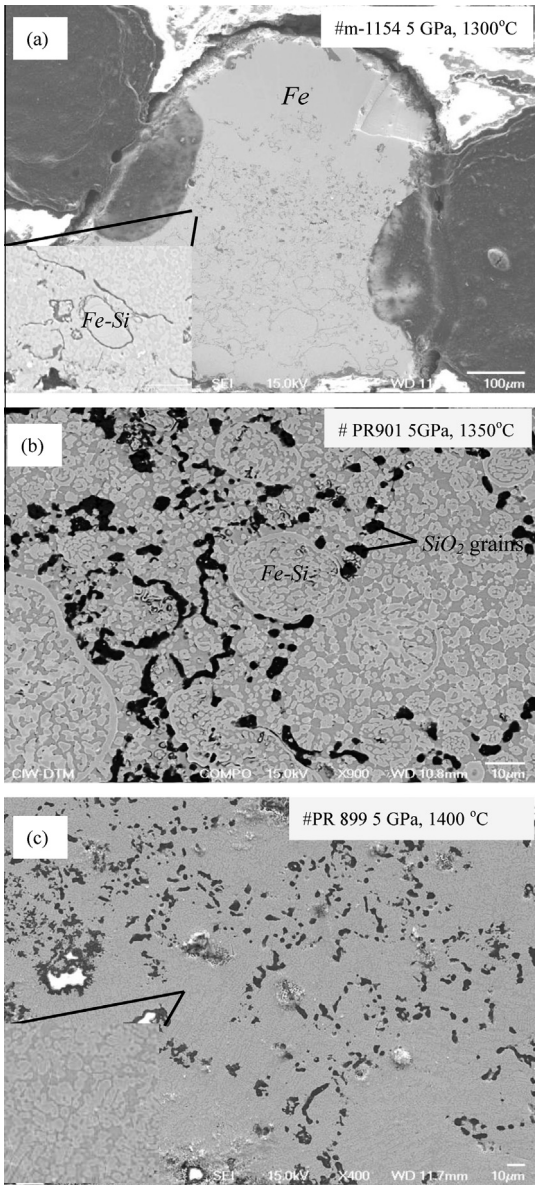

Fig. 6. Scanning electron microscope composition images of the quenched products. (a) m-1154 shows solid Fe coexisting with S rich liquid. A silicon rich droplet observed in the S rich liquid is shown in an enlarged image. (b) PR-901 shows immiscible quench texture of Si-rich droplets in S-rich matrix. Blacks are SiO_2 grains. (c) PR 899 shows one homogenous melt with dendritic texture at 5 GPa and 1400 °C, which indicates complete closure of miscibility gap.

carbon into Fe–Si–S ternary system does not significant change the closure pressure of immiscible liquids.

The liquidus temperatures at 10 GPa in the Fe–S–C–Si quaternary system are constrained between 1275 and 1350 °C (m-1164, m-1161). This is much lower than the liquidus temperatures for Fe-0.8 wt% C (1777 °C) in the Fe–C binary system at the same pressure. Therefore, Fe-multiple light elements experiments show significant modification of the melting temperature of the iron alloys.

4. DISCUSSIONS

4.1. Phase relations in Fe–S–C ternary system

By applying the topological principles described by Schreinemakers (Schreinemarkers, 1915–1925; Zen, 1966), we constructed a schematic P-T projection between 5 and 20 GPa, 1025–1300 °C for part of the Fe–S–C system (Figs. 7 and 8). For certain bulk compositions, there are at least two invariant points in this P–T range, and five unique phases for each invariant point (Fig. 8): Fe_7C_3, Fe_3C, Fe, FeS and melt for invariant point I, and FeS, Fe_3S_2, Fe, Fe_7C_3 and melt for invariant point II. Compositional degeneracy occurs at both invariant points because of the compositional collinearity:

$$3Fe_3C = Fe_7C_3 + 2Fe \text{ and } 2FeS + Fe = Fe_3S_2.$$

The coincidence rule dictates that five curves should radiate from each invariant point, but only four distinct slopes should occur due to the compositional degeneracy. For invariant point I, the four reactions are:

$$(Fe_7C_3) \quad Fe_3C + FeS + Fe \rightarrow \text{melt},$$

$$(Fe) \quad Fe_7C_3 + \text{melt} \rightarrow Fe_3C + FeS,$$

$$(FeS, \text{melt}) \quad Fe_7C_3 + Fe \rightarrow Fe_3C,$$

$$(Fe_3C) \quad Fe_7C_3 + Fe + FeS \rightarrow \text{melt}.$$

For invariant point II, the four reactions are:

$$(FeS) \quad Fe_3S_2 + Fe_7C_3 + Fe \rightarrow \text{melt},$$

$$(Fe) \quad Fe_3S_2 + Fe_7C_3 \rightarrow FeS + \text{melt},$$

$$(Fe_7C_3, \text{melt}) \quad FeS + Fe \rightarrow Fe_3S_2,$$

$$(Fe_3S_2) \quad FeS + Fe + Fe_7C_3 \rightarrow \text{melt}.$$

None of the reactions have been systematically investigated experimentally. So the position of invariant points and all reactions slopes are rough estimates based on limited experimental data. Compared with other reactions, the reactions (FeS, melt) around the invariant point I and (Fe_7C_3, melt) around the invariant point II have been relatively better constrained because of the data from this study (m-997, m-1097, m-1029, LO-707) and some experimental constraints from the materials science literature (Tsuzuki et al., 1984).

4.2. Fe–S–C planetary core

There remains a continuing interest in the liquid miscibility gap exhibited in many Fe-alloy ternary systems both for industry applications and fundamental geophysical implications (Wang et al., 1991; Raghavan, 1998; Sanloup and Fei, 2004; Corgne et al., 2008; Dasgupta et al., 2009; Tsuno and Ohtani, 2009; Morard and Katsura, 2010). The melting experiments in this study, combined with existing data, show that the miscibility gap between Fe–S and Fe–C liquids closes at 4.9 GPa with composition of Fe–C(4.35-5 wt%)–S(5-7.85 wt%). The existence of a miscibility gap in Fe–S–C ternary system can be understood in terms of bond energy considerations (Sahajwalla and Khanna, 2003). The Fe–S bond is strongly attractive and ionic in

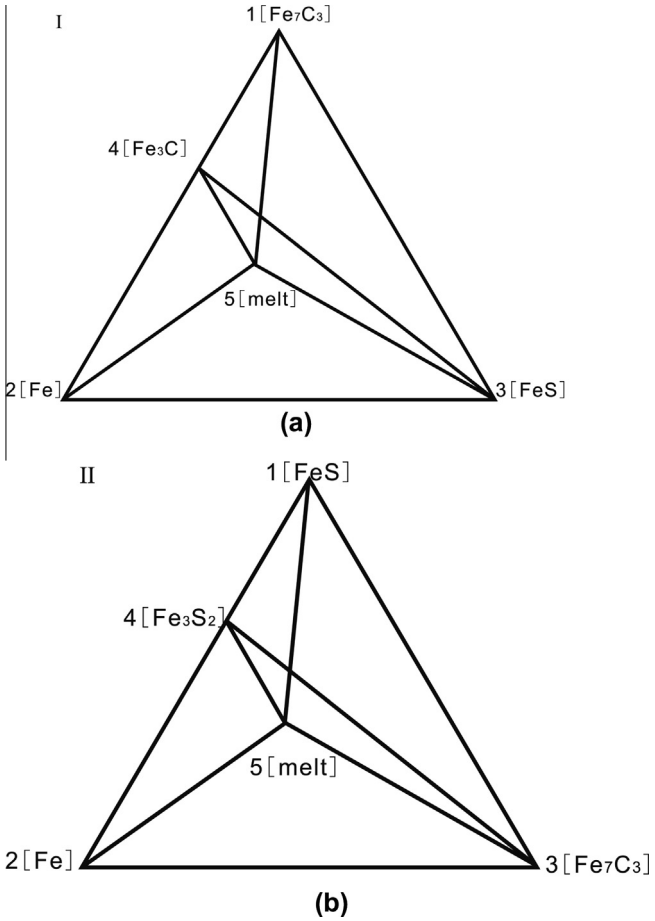

Fig. 7. Compositional topology of the five phases around the invariant point I (a) and II (b). All phases are labeled on the ternary diagrams.

nature. When a C atom tends to dissolve into a Fe atom that has a S atom in its neighborhood, the C atom will find it difficult to replace attractive C–C and Fe–S bonds with repulsive Fe–C and C–S bonds. Eventually the Fe–S melts choose an energetically favorable way to separate from the Fe–C melts.

The closure of the miscibility gap in the Fe–S–C system at high pressure is related to structural similarity evolution of the immiscible melts upon increasing pressure (Sanloup and Fei, 2004; Corgne et al., 2008; Morard et al., 2008; Tsuno and Ohtani, 2009; Dasgupta et al., 2009). It has been documented that there is no phase transformation in Fe_3C up to 30 GPa (Li et al., 2002), and hence structural change of the Fe–S component may play an important role in closing the miscibility gap (Morard et al., 2007). There is an electronic transition in FeS at about 5 GPa, leading to abrupt change in the c/a ratio and shortening Fe–Fe bond distance (Fei et al., 1995).

Because of the low eutectic melting temperature in the Fe–FeS binary system (Fei et al., 1997, 2000), S can be readily incorporated into the iron melt phase during the planetary accretion and differentiation process. Our new data in the Fe–S–C system indicate the liquidus temperature decreases significantly compared with that in the Fe–S binary system by adding a very small amount of carbon into the Fe–S system (Fig. 5). Therefore, Fe–S–C melt drops could easily transport to the core with the presence of carbon in the primitive Earth.

In addition to changing the liquidus temperature of the system, carbon also affects the solidus temperature significantly. The solidus temperature is elevated to 1100–1200 °C with the small additional amount of carbon, which is 150–250 °C higher than that in the Fe–S binary system at 5 GPa.

The composition and evolution of the iron-predominant planetary core during cooling are strictly controlled by the melting relations in the iron-light elements system. The crystallization sequence is crucial for understanding the compositional evolution of planetary cores. The cotectic boundaries between different subsolidus formations are shown in Fig. 9. At 10 GPa, the cotectic boundary between Fe_3C and Fe_7C_3 is obtained in the Fe–C–S system (Fig. 9). The carbon content at the eutectic point in the Fe–C binary system is about 3.8 wt%. The formation of an iron carbide solid inner core is dependent on the bulk carbon concentration in the core. Our results show that only a small amount of C is needed to form an iron carbide (Fe_3C or Fe_7C_3) solid inner core with the presence of S.

Mercury is the only terrestrial planet other than the Earth with a perceptible dipole magnetic field, which could indicate the presence of a partially molten iron surrounding a solid inner core. Mercury's composition is characterized by two specific features: a high density and a low surface

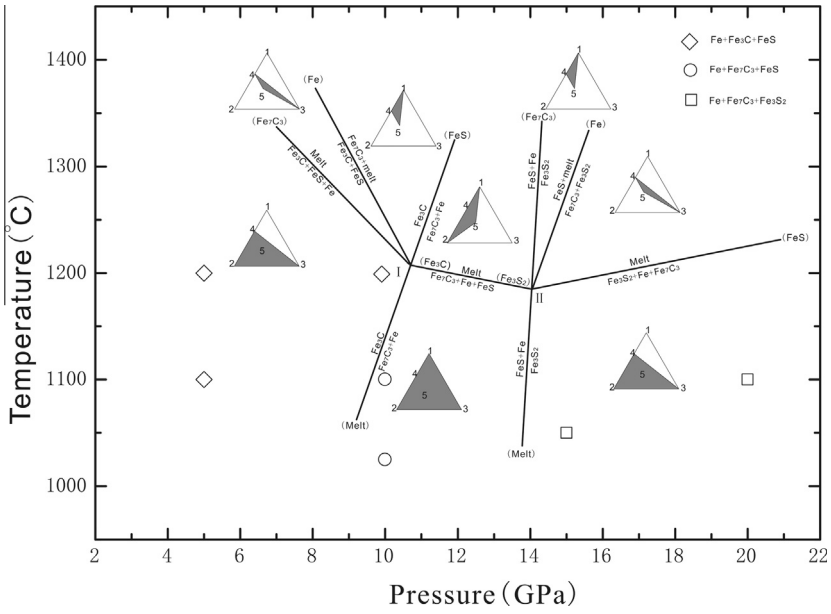

Fig. 8. Phase relation topology in the pressure range of 3.5–20 GPa and temperatures of 1000–1300 °C for the system Fe–S–C ternary system, showing sets of univariant reactions emanating from two invariant points I and II. Solid curves are the univariant lines and the corresponding reactions productions are marked along them. The phase in parentheses is the non-existent phase in the given reaction. Diamond, circle, and square represent subsolidus phases as indicated in the legend. The small ternary diagrams illustrate phase compatibility in different phase zone as illustrated in Fig. 7. The position and slope of the reaction boundaries are bracketed by our data.

FeO content (Verhoeven et al., 2009; Malavergne et al., 2010). These two features are shown to be consistent with very low oxygen fugacity during core segregation. The low oxygen fugacity is characteristic of high-iron enstatite (EH) and Bencubbinite (CB) chondrites, raising the possibility that such materials may be the important building blocks of Mercury (Wasson, 1988; Sprague et al., 1995). The C and S abundance in EH and CB chondrites are plotted in Fig. 9. Our experiments suggest that metallic iron with a small amount of dissolved carbon would be the major inner core component if EH and CB chondrites represent the composition of Mercury.

4.3. Fe–S–C–Si planetary core

Since there is no compelling reason to exclude the coexistence of multiple light elements in the Earth's core, our high pressure experiments in the Fe–S–C–Si quaternary system provide a first trial to explore the mutual solubility and crystallization behavior of a more realistic planetary core composition.

In our studied pressure range, the observed liquidus temperatures in the Fe–S–C–Si system are much lower than in the melting temperatures of pure iron. As discussed before, the miscibility gap closure has important implications for planetary differentiation and compositional stratification of a planetary core. By comparing with miscibility evolution in Fe–S–Si system reported by Morard and Katsura (2010), our experimental results show that additional a small amount of C does not play a significantly role in controlling the occurrence and closure of the miscibility gap in the Fe–S–C–Si system at high pressure. Therefore, no compositional stratification is expected for a Fe–S–C–Si Earth's core, although it may occur during early melting events.

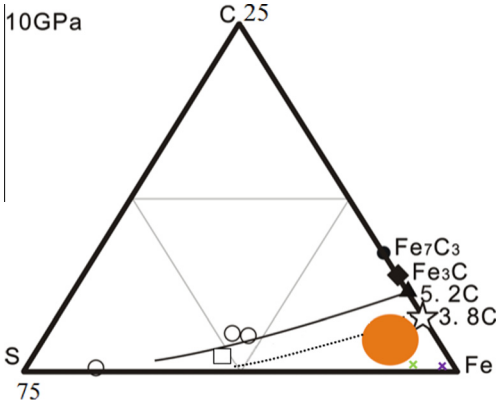

Fig. 9. The cotectic curves coexisting with solid Fe and Fe_3C (dotted line), Fe_3C and Fe_7C_3 (solid line) in the Fe–S–C ternary phase diagram. Open squares and circles represent experimental data in the first crystallization zones of Fe_3C and Fe_7C_3, respectively. Open pentagram and solid triangle represent cotectic point in Fe–C binary system at 10 GPa obtained by (Fei et al., 2007) and Nakajima et al., 2009. Fe_3C and Fe_7C_3 are also labeled on Fe–C side as solid diamond and circle. The potential compositions of the Earth's core (solid orange circle) (Ahrens and Jeanloz, 1987Li and Fei, 2003;), the C and S abundance in EH (green cross) and CB (purple cross) chondrites which are the possible building blocks of the Mercury are also indicated. (For interpretation of the references to color in this figure legend, the reader is referred to the web version of this article.)

Possible light elements such as S, Si, O, C, and H, alloying with Fe are argued to be the constituents of the terrestrial planetary cores, such as Mercury, Venus and Mars, based on model composition calculations, high pressure melting experiments, and space mission observations (Harder and Schubert, 2001; Breuer et al., 2007; Solomon et al., 2007; Stewart and Schmidt, 2007; Rivoldini et al., 2009; Morgan and Anders, 2010; Fei and Bertka, 2013). Based on our Fe–S–C–Si melting data, no layered liquid core should exist in the Mars, because of its high core pressure. The CMB pressure of Mercury is estimated to be ~7 GPa. Assuming its core is mainly composed of Fe–S–Si with small amount of carbon, a layered liquid outer core is unlikely to be expected either.

Sulfur preferentially partitions into molten iron while significant amount of Si enters the solid phase with temperature decrease. Meanwhile, the C concentration in the liquid and solid iron metal changes little with temperature variations. If S, C and Si partitioning behavior between molten and solid iron metal with temperature remains the same under Earth's present core pressure conditions, most silicon would be incorporated into the solid inner core. On the other hand, the liquid outer core will be S rich and Si poor. Moderate carbon will be evenly present in both solid and liquid cores.

ACKNOWLEDGEMENTS

This research was supported by NASA Grant to Y.F. (NNX07AF94G), and NSF grant EAR0948131 to A. S, the Carnegie Institution of Washington, the National Natural Science Foundation of China to X.L. (41090371) and 41020134003. The authors thank Angele Ricolleau and Li Zhang for help with the multi-anvil experiments. Chris Hadidiacos and John Armstrong are acknowledged for their help in acquisition of the probe data. We also thank Richard W. Carlson for fruitful discussions.

REFERENCES

Ahrens T. J. and Jeanloz R. (1987) Pyrite: shock compression, isentropic release, and composition of the Earth's core. *J. Geophys. Res.* **92**, 10363–10375.

Anderson W. W. and Ahrens T. J. (1994) An equation of state for liquid iron and implications for the Earth's core. *J. Geophys. Res.* **99**, 4273–4284.

Anderson O. L. and Isaak D. G. (2002) Another look at the core density deficit of Earth's outer core. *Phys. Earth Planet. Inter.* **131**, 19–27.

Badro J., Fiquet G., Guyot F., Gregoryanz E., Occelli F., Antonangeli D. and d'Astuto M. (2007) Effect of light elements on the sound velocities in solid iron: implications for the composition of Earth's core. *Earth Planet. Sci. Lett.* **254**, 233–238.

Bastin G. F. and Heijligers H. J. M. (1986) Quantitative electron probe microanalysis of carbon in binary carbides. *X-ray Spectrom.* **15**, 135–150.

Bertka C. M. and Fei Y. (1997) Mineralogy of the Martian interior up to core–mantle boundary pressures. *J. Geophys. Res.* **102**, 5251–5264.

Breuer D., Hauck S. A., Buske M., Pauer M. and Spohn T. (2007) Interior evolution of Mercury. *Space Sci. Rev.* **132**, 229–260.

Buono A. S. and Walker D. (2011) The Fe-rich liquidus in the Fe–FeS system from 1 bar to 10 GPa. *Geochim. Cosmochim. Acta* **75**, 2072–2087.

Chudinovskikh L. and Boehler R. (2007) Eutectic melting in the system Fe–S to 44 GPa. *Earth Planet. Sci. Lett.* **257**, 97–103.

Corgne A., Wood B. J. and Fei Y. (2008) C- and S-rich molten alloy immiscibility and core formation of planetesimals. *Geochim. Cosmochim. Acta* **72**, 2409–2416.

Dasgupta R., Buono A., Whelan G. and Walker D. (2009) High-pressure melting relations in Fe–C–S systems: implications for formation, evolution, and structure of metallic cores in planetary bodies. *Geochim. Cosmochim. Acta* **73**, 6678–6691.

Dasgupta R. and Walker D. (2008) Carbon solubility in core melts in a shallow magma ocean environment and distribution of carbon between the Earth's core and the mantle. *Geochim. Cosmochim. Acta* **72**, 4627–4641.

Dasgupta R., Chi H., Shimizu N., Buono A. S. and Walker D. (2013) Carbon solution and partitioning between metallic and silicate melts in a shallow magma ocean: implications for the origin and distribution of terrestrial carbon. *Geochim. Cosmochim. Acta* **102**, 191–212.

Fei Y. and Bertka C. M. (2013) The interior of Mars. *Science* **308**, 1120–1121.

Fei Y., Prewitt C. T., Mao H. K. and Bertka C. M. (1995) Structure and density of FeS at high pressure and high temperature and the internal structure of Mars. *Science* **268**, 1892–1894.

Fei Y., Bertka C. M. and Finger L. W. (1997) High-pressure iron–sulfur compound, Fe_3S_2, and melting relations in the Fe–FeS system. *Science* **275**, 1621–1623.

Fei Y., Li J., Bertka C. M. and Rewitt C. T. (2000) Structure type and bulk modulus of Fe_3S, a new iron–sulfur compound. *Am. Mineral.* **85**, 1830–1833.

Fei Y., Wang Y. and Deng L. (2007) Melting relations in the Fe–C–S system at high pressures: implications for the chemistry of the cores of the terrestrial planets. *Lunar and Planet. Sci. Conf. XXXVIII.* #1231 (abstr.).

Georg R. B., Halliday A. N., Schauble E. A. and Reynolds B. C. (1992) Silicon in the Earth's core. *Nature* **447**, 1102–1106.

Goldstein J., Newbury D. E., Echlin P., Joy D. C., Romig A. D., Lyman C. E., Fiori C. and Lipshin E. (1992) *Scanning Electron Microscopy and X-ray Microanalysis*. Plenum Press, New York.

Harder H. and Schubert G. (2001) Sulfur in Mercury's core? *Icarus* **151**, 118–122.

Hillgren V. J., Gessmann C. K. and Li J. (2000) *Origin of the Earth and Moon: An Experimental Perspective on the Light Element in Earth's Core*. University of Arizona Press, pp. 245–263.

Ito E., Morooka K., Ujike O. and Katsura T. (1995) Reactions between molten iron and silicate melts at high pressure: implications for the chemical evolution of Earth's core. *J. Geophys. Res.* **100**, 5901–5910.

Kuwbaschewski O. (1982) *Iron Binary Phase Diagrams*. Springer-Verlag, New York.

Kuwayama Y. and Hirose K. (2004) Phase relations in the system Fe-FeSi at 21 GPa. *Am. Mineral.* **89**, 273–276.

Kato T. and Ringwood A. E. (1989) Melting relationships in the system Fe–FeO at high pressures: implications for the composition and formation of the Earth's core. *Phys. Chem. Mineral.* **16**, 524–538.

Li J. and Fei Y. (2003) Experimental constraints on core composition. *Treatise Geochem.* **2**, 521–546.

Li J., Mao H. K., Fei Y., Gregoryanz E., Eremets M. and Zha C. S. (2002) Compression of Fe_3C to 30 GPa at room temperature. *Phys. Chem. Mineral.* **29**, 166–169.

Lord O. T., Walter M. J., Dasgupta R., Walker D. and Clark S. M. (2009) Melting in the Fe–C system to 70 GPa. *Earth Planet. Sci. Lett.* **284**, 157–167.

Lacaze J. and Sundman B. (1991) An assessment of the Fe–C–Si system. *Metall. Trans. A* **22**, 2211–2223.

McDonough W. F. (2003) Compositional model for the earth's core. *Treatise Geochem.* **2**, 547–568.

McDonough W. F. and Sun S. S. (1995) The composition of the Earth. *Chem. Geol.* **120**, 223–253.

Morgan J. W. and Anders E. (2010) Chemical composition of Earth, Venus, and Mercury. *Proc. Natl. Acad. Sci. U.S.A.* **77**, 6973–6977.

Morard G. and Katsura T. (2010) Pressure–temperature cartography of Fe–S–Si immiscible system. *Geochim. Cosmochim. Acta* **74**, 3659–3667.

Morard G., Sanloup C., Fiquet G., Mezouar M., Rey N., Poloni R. and Beck P. (2007) Structure of eutectic Fe–FeS melts up to 17 GPa: implications for planetary cores. *Earth Planet. Sc. Lett.* **263**, 128–139.

Morard G., Sanloup C., Guillot B., Fiquet G., Mezouar M., Perrillat J. P., Garbarino G., Mibe K., Komabayashi T. and Funakoshi K. (2008) In situ structural investigation of Fe–S–Si immiscible liquid system and evolution of Fe–S bond properties with pressure. *J. Geophys. Res.* **113**, B10205.

Malavergne V., Toplis M. J., Berthet S. and Jones J. (2010) Highly reducing conditions during core formation on Mercury: implications for internal structure and the origin of a magnetic field. *Icarus* **206**, 199–209.

Nakajima Y., Takahashi E., Suzuki T. and Funakoshi K. I. (2009) "Carbon in the core" revisited. *Phys. Earth Planet. Inter.* **174**, 202–211.

O'Neil H. S. C. (1991) The origin of the moon and the early history of the Earth – A chemical model. Part 1: the moon. *Geochim. Cosmochim. Acta* **55**, 1135–1157.

Poirier J. P. (1994) Light-elements in the Earth's outer core – a critical-review. *Phys. Earth Planet. Inter.* **85**, 319–337.

Pouchou J. L. (1996) Use of soft X-rays in microanalysis. *Mikrochim. Acta Suppl.* **13**, 39–60.

Raghavan V. (1998) C–Fe–S (carbon–iron–sulfur). *J. Phase Equilib.* **19**, 262–263.

Rivoldini A., Hoolst T. V. and Verhoeven O. (2009) The interior structure of Mercury and its core sulfur content. *Icarus* **201**, 12–30.

Robaut F., Crisci A., Durand-Charre M. and Jouanne D. (2006) Practical aspects of carbon content determination in carburized steels by EPMA. *Microsc. Microanal.* **12**, 331–334.

Schreinemarkers F. A. H. (1915–1925) In-, mono-, and divariant equilibria. *Proc. K. Ned. Akad. Wet. English ed., v.* 18–28.

Sprague A. L., Hunten D. M. and Lodders K. (1995) Sulfur at Mercury, elemental at the poles and sulfides in the regolith. *Icarus* **118**, 211–215.

Sahajwalla V. and Khanna R. (2003) Effect of sulfur on the dissolution behavior of graphite in Fe–C–S melts: A Monte Carlo simulation study. *Scand. J. Metall.* **32**, 53–67.

Sanloup C. and Fei Y. (2004) Closure of the Fe–S–Si liquid miscibility gap at high pressures. *Phys. Earth Planet. Inter.* **147**, 57–74.

Shahar A., Ziegler K., Young E. D., Ricolleau A., Schauble E. A. and Fei Y. W. (2009) Experimentally determined Si isotope fractionation between silicate and Fe metal and implications for Earth's core formation. *Earth Planet. Sci. Lett.* **288**, 228–234.

Shterenberg L. E., Slesarev V. N., Korsunskaya I. A. and Kamenetskay D. S. (1975) The experimental study of the interaction between melt, carbides and diamond in the iron–carbon system at high pressures. *High Temp. High Pressures* **7**, 517–522.

Solomon S. C., McNutt R. L., Gold R. E. and Domingue D. L. (2007) MESSENGER mission overview. *Space Sci. Rev.* **131**, 3–39.

Stacey F. D. and Davis M. (2008) *Physics of the Earth*. Cambridge University Press, United Kingdom.

Stewart A. J. and Schmidt M. W. (2007) Sulfur and phosphorus in the Earth's core: The Fe–P–S system at 23 GPa. *Geophys. Res. Lett.* **34**, L13201.

Tsuno K. and Ohtani E. (2009) Eutectic temperatures and melting relations in the Fe–O–S system at high pressures and temperatures. *Phys. Chem. Mineral.* **36**, 9–17.

Tsuzuki A., Sago S., Hirano S. I. and Naka S. (1984) High temperature and pressure preparation and properties of iron carbides Fe_7C_3 and Fe_3C. *J. Mater. Sci.* **19**, 2513–2518.

Verhoeven O., Tarits P., Vacher P., Rivoldini A. and Van Hoolst T. (2009) Composition and formation of Mercury: constraints from future electrical conductivity measurements. *Planet Space Sci.* **57**, 296–305.

Wasson J. T. (1988) The building stones of the planets. In *Phase Equilibria of Liquid Fe–S–C Ternary System*, vol. 31 (eds. F. Vilas, C. R. Chapman, C. Wang, J. Hirama, T. Nagasaka and S. Banya). ISIJ International, pp. 1292–1299.

Wang C., Hirama J., Nagasaka T. and Banya S. (1991) Phase equilibria of liquid Fe-SC ternary system. *ISIJ international* **31**, 1292–1299.

Wänke H. and Dreibus G. (1997) New evidence for silicon as the major light element in the Earth's core. *Lunar Planet. Sci. Conf. XXVIII*. pp. 1280.

Wood B. J. (1993) Carbon in the core. *Earth Planet. Sci. Lett.* **117**, 593–607.

Zen E.-A. (1966) Construction of pressure–temperature diagrams for multicomponent systems after the method of Schreinemakers – a geometric approach. *Geol. Survey Bull.* **1225**, 33–44.

Associate editor: Frederic Moynier